Baroclinic vortex influence on wave drag reduction induced by pulse energy deposition

doi: 10.1063/1.3147932

Baroclinic vortex influence on wave drag reduction induced by pulse energy deposition

Yousuke Ogino,[a] Naofumi Ohnishi, Shinichi Taguchi,[b] and Keisuke Sawada
Department of Aerospace Engineering, Tohoku University, 6-6-01 Aramaki-Aza-Aoba, Aoba-ku, Sendai 980-8579, Japan

(Received 16 September 2008; accepted 2 May 2009; published online 15 June 2009)

We present the results of numerical analysis of wave drag reduction by a single-pulse energy deposition in a supersonic flow field around a sphere. The wave drag for the sphere was reduced as a result of the interaction between a low-density core following the blast wave produced by the energy deposition and the bow shock developed in front of the sphere. We investigated the drag reduction mechanism in terms of the unsteady flow field induced by the interaction. The effects of deposited energy and deposition location on energy reduction were examined by parametric study. From the obtained results, we refined the parameters, utilizing the baroclinic source term that produced vorticity in the vortex equation when the gradients of density and pressure were not parallel. The baroclinic vortex driven by Richtmyer–Meshkov-like instability was strong enough to contribute to the temporary low-entropy shock formation that caused low wave drag for the supersonic object. We determined that the reduced energy had a linear dependence on the radius of the low-density core formed in the blast wave and was proportional to the square of the freestream Mach number. Such dependencies could be predicted with the assumption that the energy was consumed by the baroclinic vortex generation and advected downward without thermalization in an inviscid shock layer. © *2009 American Institute of Physics*. [DOI: 10.1063/1.3147932]

I. INTRODUCTION

The bow shock developed in front of a blunt body in a supersonic flow field is the origin of troublesome wave drag. Reducing wave drag improves the fuel efficiency and operating flexibility of a supersonic vehicle. Many researchers have studied wave drag reduction in supersonic vehicles by using both structural and nonstructural methods to control the flow field ahead of the vehicle. A typical structural method involves attaching a physical spike to the body nose.[1–3] The spike forms a conical shock wave that changes the flow direction outward, significantly reducing the drag of the body. However, some problems occur in the practical application of this method. The spike has to endure a large heat flux at the apex, as well as the pitching moment generated in the flight with a finite angle of attack. In order to avoid these problems, nonstructural methods of drag reduction have been investigated; these methods use energy deposition instead of the physical spike.[4–7] Continuously supplying energy using a continuous wave laser ahead of the blunt body forms a conical shock wave, and the drag of the body is reduced as well as with the physical spike method.

In the past decade, a supersonic flow control method using pulsed-laser deposition was proposed and investigated experimentally and numerically.[8–14] With this method, the pulse energy supplied ahead of a bow shock formed over a blunt body generates a blast wave, which interacts with the bow shock (Fig. 1). Adelgren *et al.*[9] demonstrated the possible application of laser-induced energy deposition to control the flow over an isolated sphere. These experiments demonstrated the effectiveness of laser-induced energy deposition in reducing surface pressure: the peak value was reduced by 30%, compared to the value observed without energy deposition. Georgievsky and Levin[12,13] and Zheltovodov *et al.*[14] performed numerical calculations in the framework of the Euler equations, using quasisteady and periodic pulsed-energy depositions that stimulated drag reduction, in order to examine the possibility of control by the normal bow shock and conical shock waves in the vicinity of blunt and sharp bodies.

Kandala and Candler[8] investigated blast wave generation by laser absorption, and the interaction between the blast wave and the bow shock over a sphere with three-dimensional thermochemical nonequilibrium Navier–Stokes computations. They confirmed that the peak of the surface pressure was significantly reduced as a result of this interaction. For practical purposes, it is still necessary to consider the characteristic mechanisms under the disturbed unsteady bow shock in order to predict quantitatively how much the pulse energy deposition reduces the drag. Also, finding the optimal condition for obtaining the most effective drag reduction will be useful.

In an inviscid flow, the wave drag originates from only the entropy production due to the shock wave; therefore, it can be assumed that drag reduction comes from any mechanism that effectively achieves a low-entropy bow shock. Since a shock wave should satisfy the Rankine–Hugoniot condition in a steady flow, an unsteady shock wave, including vortices behind it, may suppress the entropy jump at the (time-averaged) shock front. If any density perturbations are supplied in front of the bow shock, the vortex must be gen-

[a]Electronic mail: yogi@rhd.mech.tohoku.ac.jp.
[b]Present address: Engineer, Kawasaki Heavy Industries Ltd., Kakamigahara 504-0971, Japan.

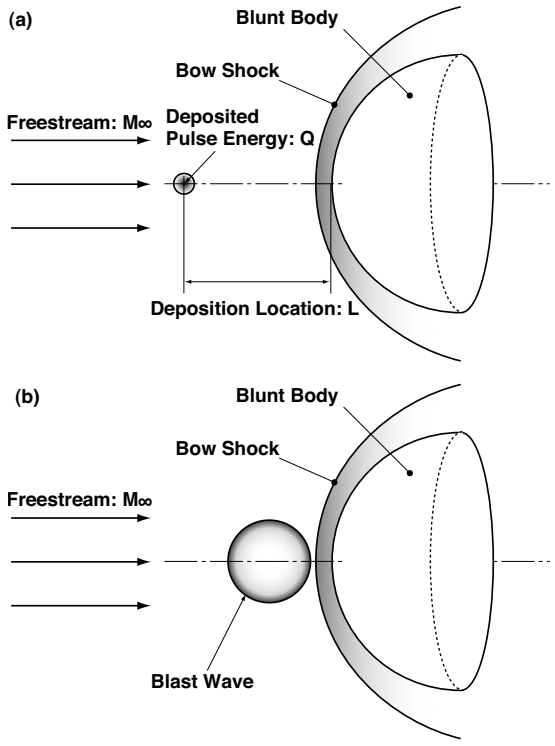

FIG. 1. Schematics of pulse energy deposition (a) just after the energy deposition and (b) before the interaction.

erated at the shock front, due to Richtmyer–Meshkov-like instability[15,16] (i.e., the baroclinic effect[17]). In the blast wave induced by pulse energy deposition, a low-density core corresponding to the contact surface of the plasma is developed as the preceding shock wave expands and has a steep gradient at the surface. This may be a seed for the baroclinic vortex and may consequently lead to the reduction of wave drag by temporarily suppressing the entropy production of the bow shock wave.

In this study, we numerically simulated of the interaction between a blast wave generated by pulse energy deposition and a bow shock developed in front of a sphere, in order to analyze the drag reduction by energy deposition. We focused on the purely hydrodynamic effect on drag reduction (i.e., the mechanism of the drag reduction by pulse energy deposition in an ideal gas). In addition, we performed parametric studies of deposited energy, deposition location, and freestream Mach number in an effort to find their dependencies on reduced energy and to obtain a physical interpretation from the perspective of baroclinic vortex generation.

II. NUMERICAL PROCEDURE

A. Governing equations and numerical methods

We considered a situation in which a bow shock is formed around a sphere in an inviscid supersonic flow, and a point source due to energy deposition generates a blast wave in a uniform flow ahead of the bow shock. The flow field around the sphere was computed by axisymmetric Euler equations written as

$$\frac{\partial \boldsymbol{Q}}{\partial t} + \frac{\partial \boldsymbol{E}}{\partial x} + \frac{\partial \boldsymbol{F}}{\partial y} + \frac{\boldsymbol{H}}{y} = 0, \tag{1}$$

where $\boldsymbol{Q}$ is the vector of conservative variables, $\boldsymbol{E}$ and $\boldsymbol{F}$ are the flux vectors, and $\boldsymbol{H}$ is the vector that comes from the axisymmetric formulation given by

$$\boldsymbol{Q} = \begin{pmatrix} \rho \\ \rho u \\ \rho v \\ e \end{pmatrix}, \quad \boldsymbol{E} = \begin{pmatrix} \rho u \\ \rho u^2 + P \\ \rho uv \\ (e+P)u \end{pmatrix},$$

$$\boldsymbol{F} = \begin{pmatrix} \rho v \\ \rho uv \\ \rho v^2 + P \\ (e+P)v \end{pmatrix}, \quad \boldsymbol{H} = \begin{pmatrix} \rho v \\ \rho uv \\ \rho v^2 \\ (e+P)v \end{pmatrix}. \tag{2}$$

Here, ρ is density, u is velocity in the x-direction, v is velocity in the y-direction, e is total energy, and P is pressure.

Because laser energy is absorbed by a very small volume of gas, a finer resolution was needed to capture the blast wave propagation in the early stage after its generation. Therefore, as a preprocess for the axisymmetric calculation, the initial blast wave propagation was computed separately by solving the spherically symmetric Euler equations written as

$$\frac{\partial \boldsymbol{U}}{\partial t} + \frac{\partial \boldsymbol{A}}{\partial r} + \frac{\boldsymbol{B}}{r} = 0, \tag{3}$$

where $\boldsymbol{U}$ is the vector of conservative variables, $\boldsymbol{A}$ is the flux vector, and $\boldsymbol{B}$ is the vector from the spherical formulation defined by

$$\boldsymbol{U} = \begin{pmatrix} \rho \\ \rho u_r \\ e \end{pmatrix}, \quad \boldsymbol{A} = \begin{pmatrix} \rho u_r \\ \rho u_r^2 + P \\ (e+P)u_r \end{pmatrix}, \quad \boldsymbol{B} = \begin{pmatrix} 2\rho u_r \\ 2\rho u_r^2 \\ 2(e+P)u_r \end{pmatrix}, \tag{4}$$

where u_r is radial velocity.

The governing equations were discretized by the cell-centered finite-volume method. Numerical flux was evaluated by the AUSM-DV upwind scheme.[18] Second-order spatial accuracy was attained by using the MUSCL extrapolation method.[19] Time integration was implemented by a second-order Runge–Kutta method.

B. Evaluation of drag reduction and efficiency

In order to assess the performance of the drag reduction scheme, the drag D of the body was determined by integrating the pressure on the frontal area of the sphere. The amount of impulse reduction was evaluated by $I(t)$:

$$\Delta I(t) = \int_0^t (D_0 - D(\tau))d\tau, \tag{5}$$

$$E_p = u_\infty \Delta I(\infty), \tag{6}$$

where D_0 is the drag in the steady state and u_∞ is the freestream velocity in the x-direction. The efficiency of the drag reduction was evaluated by E_p/Q, where E_p is the re-

duced propulsion energy of the body defined by Eq. (6) and Q is the deposited energy.

C. Normalization of variables

Since all computations were performed in the framework of the Euler calculations, the quantities could be normalized. We defined the characteristic parameters as the diameter of the sphere d, the freestream pressure P_∞, and the sound speed c_∞, which are derived from dimensional analysis. The quantities are normalized and redefined as

$$x = \frac{\bar{x}}{d}, \quad y = \frac{\bar{y}}{d}, \quad r = \frac{\bar{r}}{d}, \quad t = \frac{\bar{t}}{d/c_\infty}, \tag{7}$$

$$u = \frac{\bar{u}}{c_\infty}, \quad v = \frac{\bar{v}}{c_\infty}, \quad u_r = \frac{\bar{u}_r}{c_\infty}, \tag{8}$$

$$\rho = \frac{\bar{\rho}}{\rho_\infty} = \frac{\bar{\rho}}{\gamma P_\infty / c_\infty^2}, \quad P = \frac{\bar{P}}{\gamma P_\infty}, \quad e = \frac{\bar{e}}{\gamma P_\infty}, \tag{9}$$

$$D = \frac{\bar{D}}{\gamma P_\infty d^2}, \quad M_\infty = \frac{\bar{u}_\infty}{c_\infty}, \quad L = \frac{\bar{L}}{d}, \tag{10}$$

$$Q = \frac{\bar{Q}}{\gamma P_\infty d^3}, \quad E_p = \frac{\bar{E}_p}{\gamma P_\infty d^3}, \quad R = \frac{\bar{R}}{d}, \quad \delta = \frac{\bar{\delta}}{d}, \tag{11}$$

$$P_{\text{bow}} = \frac{\bar{P}_{\text{bow}}}{P_\infty}, \quad \rho_{\text{low}} = \frac{\bar{\rho}_{\text{low}}}{\rho_\infty}, \tag{12}$$

$$\omega_z = \frac{\bar{\omega}_z}{c_\infty / d}, \quad E_v = \frac{\bar{E}_v}{\gamma P_\infty d^3}. \tag{13}$$

Here, the overbar denotes dimensional variables, u_∞ is the freestream velocity, M_∞ is the freestream Mach number, L is the deposition location, R is the low-density radius, δ is the shock stand-off distance, P_{bow} is the pressure behind bow shock, ρ_{low} is the density at the radius R in the low-density region, ω_z is the vorticity, and E_v is the vortex energy.

D. Simulation conditions

Pulse energy deposition was assumed to be absorbed instantly by a spherical region with the radius of 10^{-2}. The initial energy distribution was given by a Gaussian distribution with a full width at half maximum of 10^{-2}. Two-ninths of the absorbed energy was assumed to turn into the kinetic energy of the blast wave to reproduce an ideal self-similar solution, even with the finite-volume energy deposition.[20] An ideal gas with $\gamma = 1.4$ was assumed in the present study. For the parametric study, the values of the freestream Mach number M_∞, the deposited energy Q, and the deposition location L were chosen as indicated in Table I. Typical computations were carried out using 301×1025 grid points for the axisymmetric simulations and 4001 grid points for the spherical simulations. This number of points for the axisymmetric simulations was required to evaluate the drag of the object over the entire simulation time. The large number of grid points for the spherical simulations ensured the accurate reproduction of the blast wave, which grows rapidly, especially in the early stage after the energy deposition.

TABLE I. Simulation conditions.

Freestream Mach number M_∞	1.6, 2.2, 2.8, 5.0, 7.3, 11.0
Deposition location L	0.3, 0.5, 0.7, 1.0
Deposited energy $Q \times 10^{-3}$	1.43, 2.86, 4.29, 7.14, 14.3

III. RESULTS AND DISCUSSION

A. Interaction between the blast wave and the bow shock

Pulse energy was deposited ahead of the bow shock and made a spherical blast wave traveling toward the bow shock along the freestream. For Secs. III A and III B, it was valuable to observe the flow field induced by the interaction between the blast wave and the bow shock from the morphological point of view. Figures 2–4 depict snapshots of the pressure, the density, and the z-direction vorticity contours at various time points, respectively. The simulation condition was set with the parameters of $M_\infty = 5$, $Q = 4.29 \times 10^{-3}$, and $L = 0.5$ (the reference condition). The pressure was normalized by the freestream value and the specific heat ratio, and negative vorticity indicates a clockwise vortex. When the front of the expanding shock wave arrived at the standing bow shock, the interaction between the blast wave and the bow shock started at $t = 0.055$ [Figs. 2 and 3; (a)]. The shell of the blast wave was compressed when the blast wave impinged on the bow shock and reflected at the wall at $t = 0.089$ [Figs. 2 and 3; (b)], where the peak of the surface pressure appeared near the stagnation point. At the same time, the low-density core of the blast wave reached the shock layer, and the gas in the shock layer was pulled upstream. As a result, the bow shock wave near the stagnation line was severely distorted; behind it, a low-pressure region shrouded by the relatively high-pressure gas was formed. This shock deformation led to a vortex sheet [Fig. 4(b)]. Meanwhile, the high-pressure region behind the distorted shock grew in size and in absolute value [Fig. 2(c)]. Concurrently, the low-density region approached the wall, and the vortex sheet gradually transformed into a vortex ring (a point in a two-dimensional view). As time elapsed, the vortex region moved and attached to the wall in the downward flow, as indicated at $t = 0.219$ in Fig. 4(e). Islands of high and low pressure (also density) then appeared in the vicinity of the vortex region [Figs. 2–4; (e)]. The profile in the pressure and density moved downstream, associated with the travel of the vortex region [Figs. 2–4; (f) and (g)], and the flow field gradually regained a steady state [Figs. 2–4; (h)]. Since the flow can be considered as almost incompressible in the shock layer, the vortex ring should remain because of the Euler computation, excluding any physical dissipations. In order to capture the low-pressure bump originating from the vortex ring, we focused on reducing the numerical dissipation by increasing the grid points because it significantly affected the

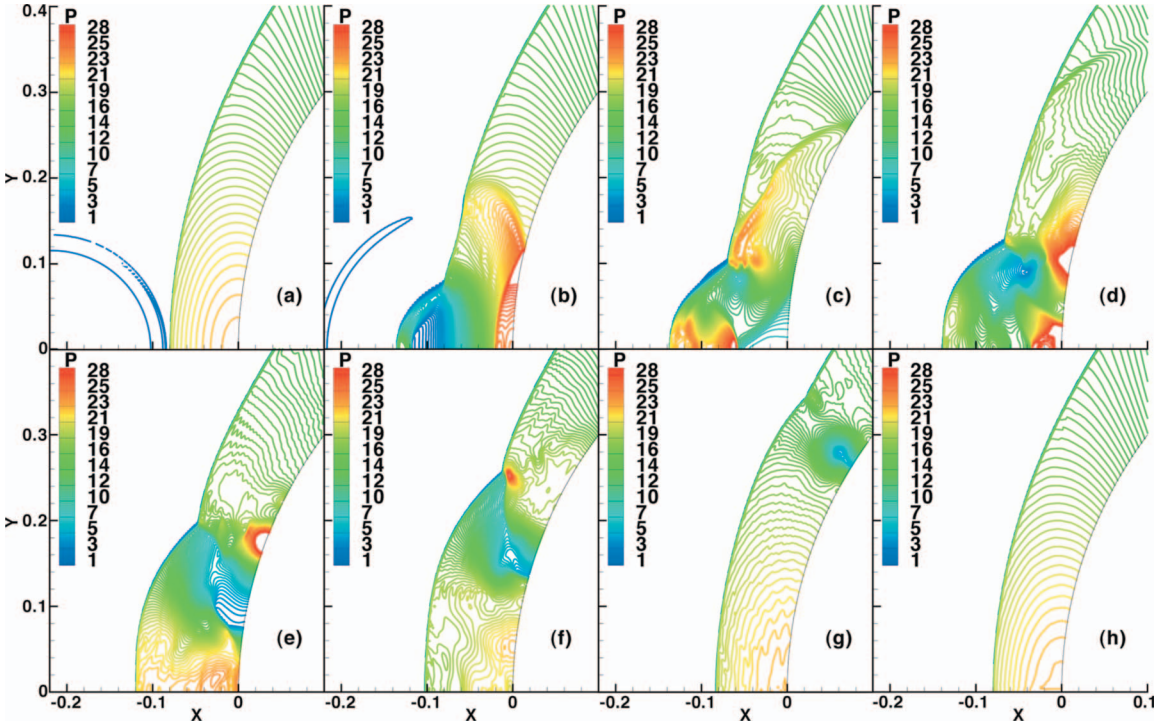

FIG. 2. (Color) Pressure P contours with the parameters of $M_\infty=5$, $Q=4.29\times10^{-3}$, and $L=0.5$ at (a) $t=0.055$ (before interaction), (b) $t=0.089$ (time of the first maximum drag), (c) $t=0.120$ (time of the first minimum drag), (d) $t=0.144$ (time of the second maximum drag), (e) $t=0.219$ (near the vortex attachment), (f) $t=0.325$, (g) $t=0.513$, and (h) $t=0.684$.

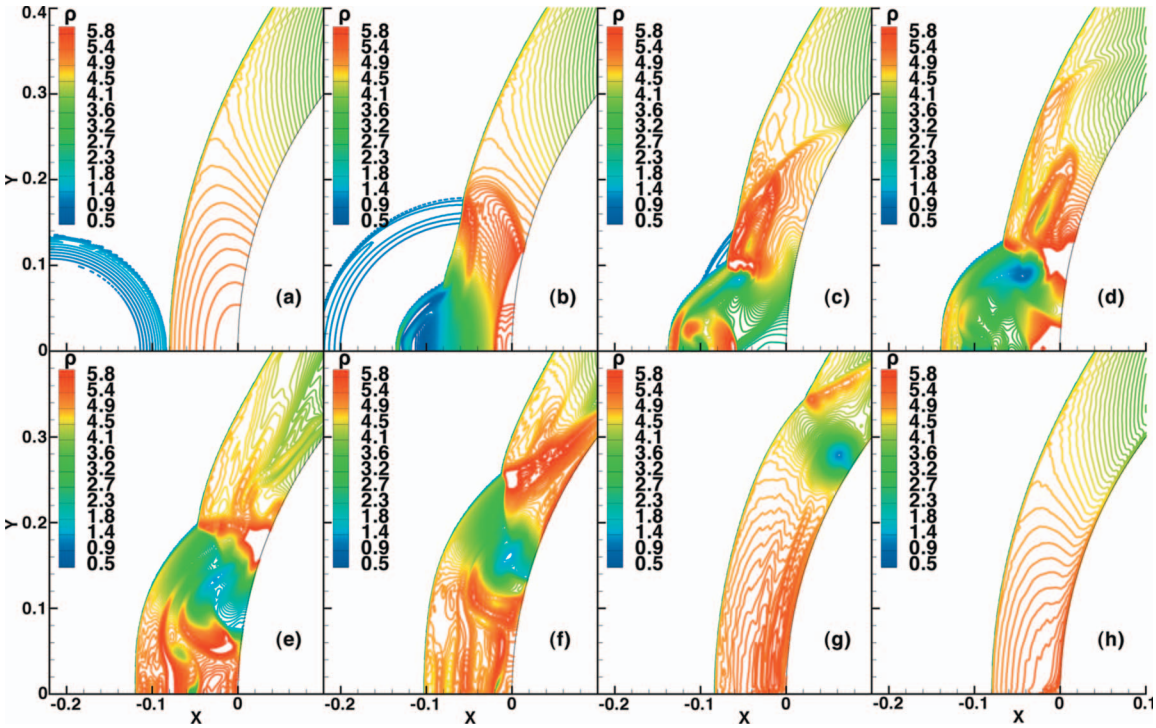

FIG. 3. (Color) Density ρ contours with the parameters of $M_\infty=5$, $Q=4.29\times10^{-3}$, and $L=0.5$ at (a) $t=0.055$ (before interaction), (b) $t=0.089$ (time of the first maximum drag), (c) $t=0.120$ (time of the first minimum drag), (d) $t=0.144$ (time of the second maximum drag), (e) $t=0.219$ (near the vortex attachment), (f) $t=0.325$, (g) $t=0.513$, and (h) $t=0.684$.

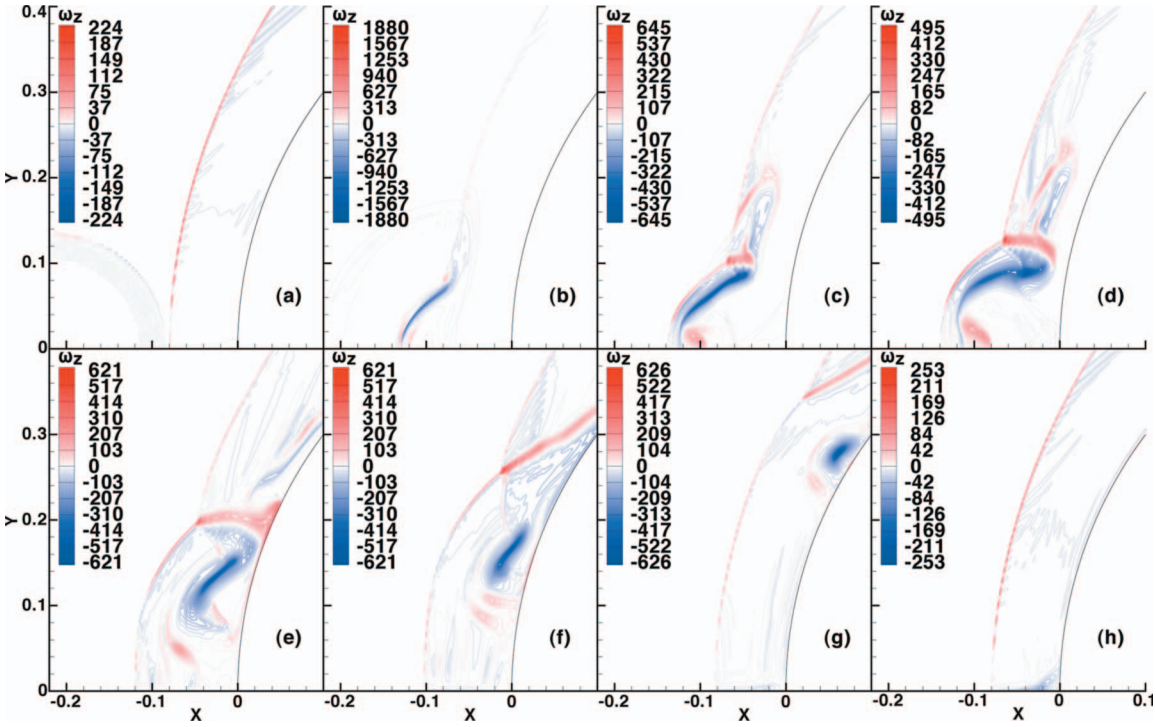

FIG. 4. (Color) z-vorticity ω_z contours with the parameters of $M_\infty=5$, $Q=4.29\times10^{-3}$, and $L=0.5$ at (a) $t=0.055$ (before interaction), (b) $t=0.089$ (time of the first maximum drag), (c) $t=0.120$ (time of the first minimum drag), (d) $t=0.144$ (time of the second maximum drag), (e) $t=0.219$ (near the vortex attachment), (f) $t=0.325$, (g) $t=0.513$, and (h) $t=0.684$.

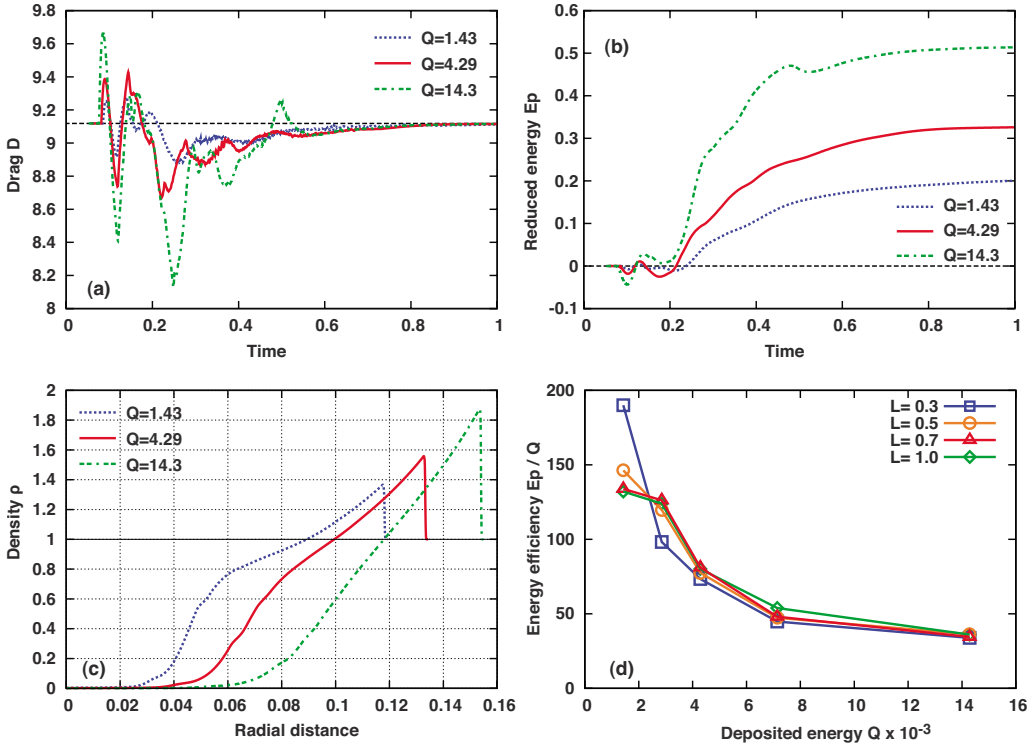

FIG. 5. (Color online) Effect of deposited energy Q. (a) Time histories of drag at $M_\infty=5$, $L=0.5$. (b) Time histories of reduced energy E_p at $M_\infty=5$, $L=0.5$. (c) Density distributions of blast wave before interaction at $M_\infty=5$, $L=0.5$. (d) Energy efficiency E_p/Q.

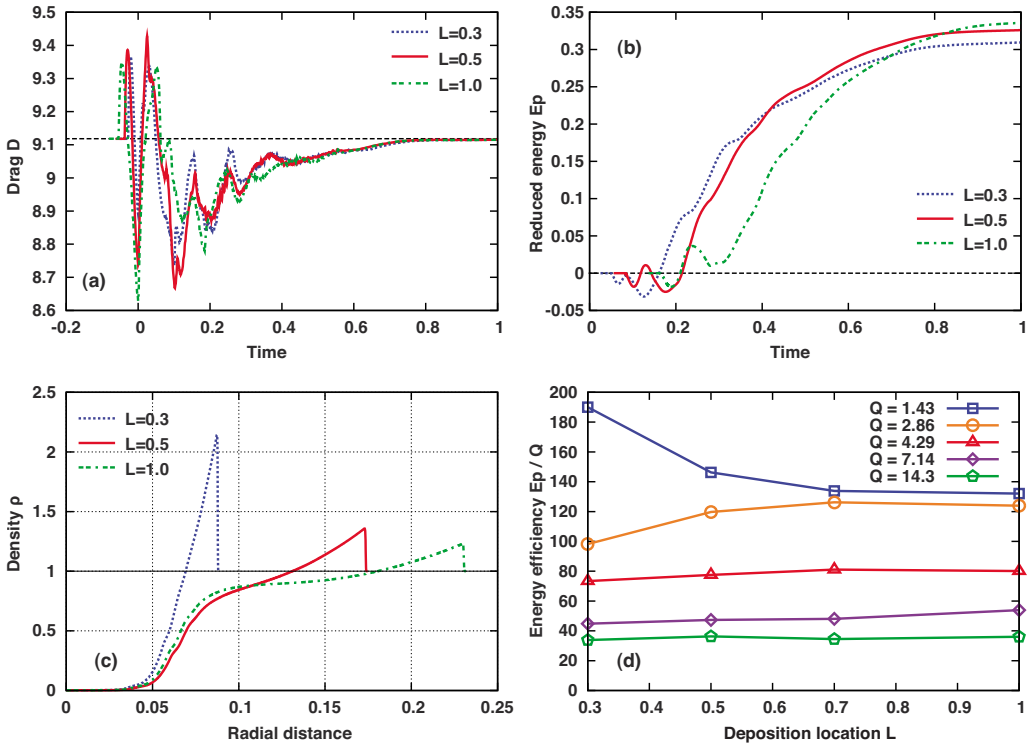

FIG. 6. (Color online) Effect of deposition location L. (a) Time histories of drag at $M_\infty=5$, $Q=4.29\times10^{-3}$. (b) Time histories of reduced energy E_p at $M_\infty=5$, $Q=4.29\times10^{-3}$. (c) Density distributions of blast wave before interaction at $M_\infty=5$, $Q=4.29\times10^{-3}$. (d) Energy efficiency E_p/Q.

wave drag of the object. Thus, the number of grids introduced in Sec. II D was relatively large even though the flow pattern was not complex.

B. Evaluation of the drag reduction

The time histories of the drag and reduced energy for the reference condition are denoted by solid lines in Figs. 5(a) and 5(b). The drag exhibited large oscillations until $t=0.3$ after the interaction began [Fig. 5(a)]. Large peaks of the drag appeared at $t=0.089$ and 0.144 when the high-pressure region stuck to the surface [Figs. 2(b) and 2(d)]. In contrast, when the low-pressure region stayed on the wall surface, the drag time history displayed valleys at $t=0.120$ and 0.219. The first valley at $t=0.120$ indicated that "lightweight gas" moved to the blunt body and reduced the drag force independently of the vortex generation. After the second valley at $t=0.219$, the drag remained below the initial drag for a while due to advection of the vortex region along the body surface. These results revealed that most of the reduced energy (i.e., the time integration of drag) was obtained between $t=0.2$ and 0.8 [Fig. 5(b)] because the vortices lowered the pressure and consequently reduced the wave drag over the object behind the bow shock. Therefore, we concluded that the vortex region formed by the interaction between the bow shock and the laser-induced low-density core was the dominant contributor to drag reduction.

C. Effect of the energy deposition conditions

Before referring to the quantitative estimate of the vortex role in drag reduction, we summarized the parametric computations. It was also helpful to determine whether optimal conditions existed within the prepared parameters. Calculations were made for various energy deposition conditions. We compared the density profiles of the blast wave just before the interaction with the bow shock began for several conditions of Q [Fig. 5(c)]. Note that the wave front of the blast wave corresponds to the position of bow shock wave surface in this figure. The low-density region extended as the deposited energy Q increased. When the low-density region was not large enough to distort the bow shock, the drag reduction was relatively small [Figs. 5(a) and 5(b)]. Moreover, it seemed that all interaction flow fields caused by different deposited energies developed in almost the same way. Figure 5(d) presents the variations of E_p/Q at $M_\infty=5$ when the deposited energy Q was varied. It was expected that a larger Q would trigger the stronger vortex formation; however, it seemed that an excessively large Q did not effectively reduce the drag.

Figure 6(d) depicts variations of E_p/Q with various values of the energy deposition location L. The profiles of E_p/Q had no optimal values for any deposition location. Regardless of whether the deposition location was close to or far from the body, the low-density region inside the blast wave shell was still a comparable size because only a short time elapsed after the energy deposition for all cases [Figs. 6(a)–6(c)]. If a blast wave propagated for a certain time, the low-density region inside the blast wave stopped growing and gradually shrank with further propagation.[20] Thus, the reduced energy E_p had no maximum value when the deposition location was varied. As indicated above, the deposition location contributed less to the reduced energy because the low-density region was still a comparable size. In addition, we found that the shock speed of the blast wave front con-

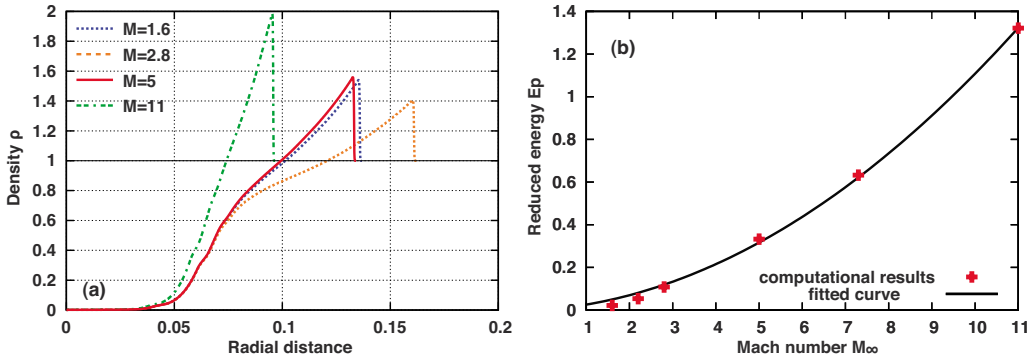

FIG. 7. (Color online) Effect of freestream Mach number M_∞ with the parameters of $Q=4.29\times10^{-3}$ and $L=0.5$. (a) Density distributions of blast wave before interaction and (b) reduced energy E_p.

tributed less to the interaction mechanism causing drag reduction, although the shock speed became high as the deposition location approached the body surface.

Figure 7(b) presents the obtained values of E_p for the various freestream Mach numbers under constant energy deposition conditions. Reduced energy E_p was found to be proportional to the square of the freestream Mach number, whereas the low-density region was almost the same size as that presented in Fig. 7(a).

D. Parameter refinement for reduced energy E_p

Parametric study results indicated that the drag was reduced more if the low-density vortex region moving along the wall surface was larger or the Mach number was higher. Thereafter, we focused on the baroclinic source term of vorticity, in order to refine the parameters for the reduced energy E_p. The baroclinic term is a well-known source of the vorticity frequently induced by hydrodynamic instabilities related to the shock wave (i.e., Richtmyer–Meshkov instability).

By taking the curl of the equation of motion for a perfect fluid

$$\frac{\partial \boldsymbol{u}}{\partial t} + \boldsymbol{u}\cdot(\nabla \boldsymbol{u}) = -\frac{1}{\rho}\nabla P, \tag{14}$$

we obtain the well-known vorticity equation

$$\frac{\partial \boldsymbol{\omega}}{\partial t} + \boldsymbol{u}\cdot(\nabla \boldsymbol{\omega}) = (\boldsymbol{\omega}\cdot\nabla)\boldsymbol{u} - \boldsymbol{\omega}(\nabla\cdot\boldsymbol{u}) + \frac{1}{\rho^2}\nabla\rho\times\nabla P, \tag{15}$$

for the vorticity vector $\boldsymbol{\omega}=\nabla\times\boldsymbol{u}$. The left-hand side of Eq. (15) is the advective derivative of $\boldsymbol{\omega}$. The right-hand side contains the terms playing roles in vorticity transport. The first term represents the stretching and warping of the vorticity tubes (it vanishes in the two-dimensional case), the second term accounts for the compressibility effect and the last term describes the baroclinic effects that generate the vorticity when a density gradient vector is not aligned parallel to a pressure gradient. Since compressibility may not become large in the shock layer, we concentrated on the baroclinic effect to estimate the absolute value of vorticity formed by the interaction between the bow shock layer and the laser-induced low-density core.

$$\frac{D\boldsymbol{\omega}}{Dt} \cong \frac{1}{\rho^2}\nabla\rho\times\nabla P. \tag{16}$$

If we used a rough estimate for these terms and assume that the gradient of density is determined by only the low-density core and that the gradient of pressure depends on the bow shock strength and the scale length of the core, we could write this equation as

$$\frac{\omega_z}{\Delta t} = \frac{1-\rho_{\mathrm{low}}}{R}\frac{P_{\mathrm{bow}}-1/\gamma}{R}. \tag{17}$$

We then obtain an estimated nondimensional vorticity that may be produced by the baroclinic term through the interaction of the bow shock and the low-density core:

$$\omega_z = \frac{\delta}{M_\infty}\frac{(1-\rho_{\mathrm{low}})(P_{\mathrm{bow}}-1/\gamma)}{R^2}, \tag{18}$$

where the subscript *low* is the low-density region inside the blast wave, *bow* is the bow shock layer, and ∞ is the freestream. Figure 8 presents a schematic of the flow field around the sphere (a) before the interaction and (b) during vorticity generation. Although the shock wave preceding the low-density core first met with the bow shock, we assumed that the resulting vortex was mainly created by the following low-density core [Fig. 8(b)], in which the preceding shock wave had already spread out. The low-density radius R was determined by the position corresponding to the maximum value of $1/\rho^2\nabla\rho$. We also estimated the characteristic interaction time Δt as δ/M_∞. Figure 9 depicts the relationship among vorticity-generating time (a computed time interval between the beginning of the interaction of the low-density core with the bow shock and the time of the maximum circulation integrated in all computational domains), shock stand-off distance δ, and low-density radius R with various Mach numbers. Because the vorticity-generating time is nearly independent of the low-density radius R, the characteristic time scale Δt was assumed to be δ/M_∞. We opted to estimate the density gradient as the difference between ambient gas density $\rho_\infty(=1)$ and density at the radius R, $\rho_{\mathrm{low}}(=\rho(R))$ over the radius R; we estimated the pressure as the difference between the pressure behind bow shock P_{bow} and ambient pressure $P_\infty(=1/\gamma)$ over the radius R [Fig. 8(b)].

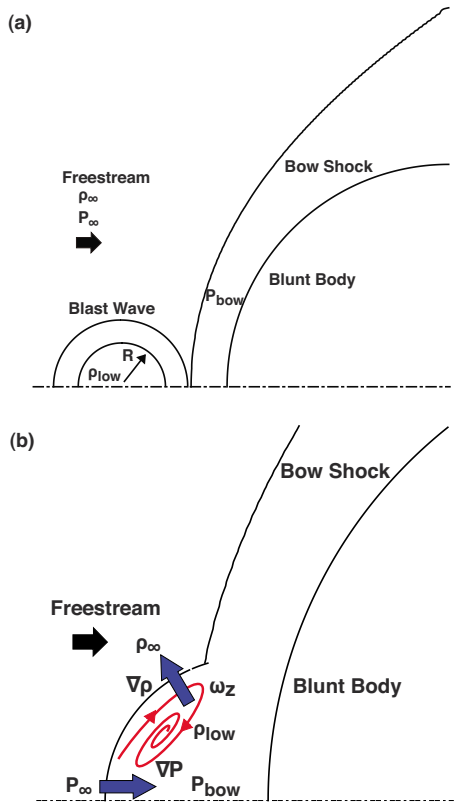

FIG. 8. (Color online) Schematics of flow field around the sphere (a) before the interaction and (b) during vorticity generation.

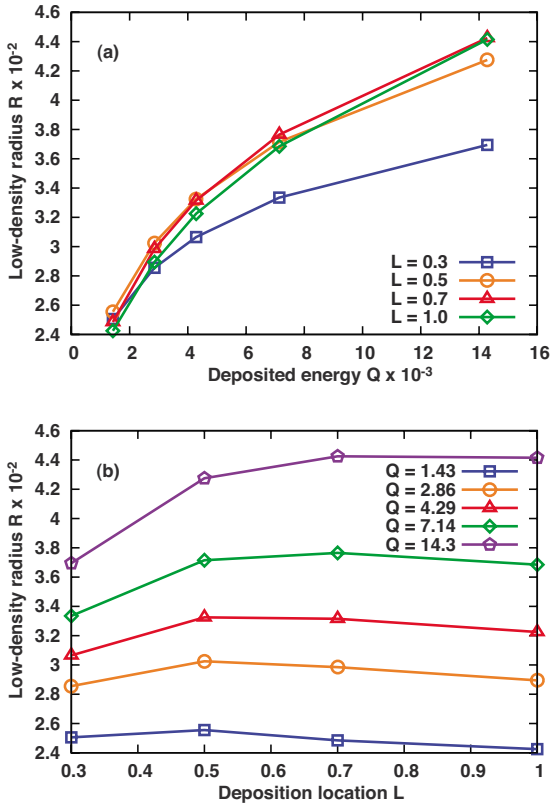

FIG. 10. (Color online) Relationship between low-density radius R and energy deposition conditions at $M_\infty=5$. (a) Deposited energy Q and (b) deposition location L.

For comparison with the reduced energy E_p, as a practical convenience we defined vortex energy E_v as

$$E_v \equiv \frac{1}{2}\omega_z^2 S_{\text{low}} V_{\text{low}} = \frac{2}{3}\left(\frac{\pi\delta}{M_\infty}\right)^2 (1-\rho_{\text{low}})^2 (P_{\text{bow}} - 1/\gamma)^2 R, \tag{19}$$

where S_{low} represents the cross-section area and V_{low} represents the volume of the low-density core. As indicated in Eq. (19), the vortex energy E_v is proportional to the low-density radius R. Figures 10(a) and 10(b) illustrate the relationship between the obtained results of the low-density radius immediately before the interaction and deposition conditions at the constant Mach number $M_\infty=5$. According to the blast wave theory with counterpressure, the large deposited energy Q leads to a more extensive low-density region, whereas it is less affected by deposition location L. A comparison of reduced energy and vortex energy is presented in Fig. 11. The crosses indicate the computational results of the reduced energy for each deposition condition, and the circles indicate the value of αE_v, where $\alpha=14.5$ is the estimated factor obtained from our computations. From the results, we may roughly represent the value of E_p by

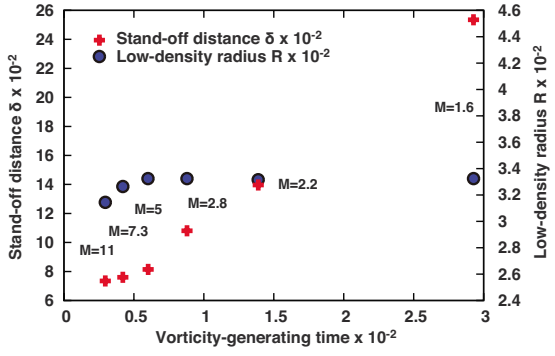

FIG. 9. (Color online) Relationship among vorticity-generating time, shock stand-off distance δ, and low-density radius R with the parameters of $Q=4.29\times10^{-3}$ and $L=0.5$.

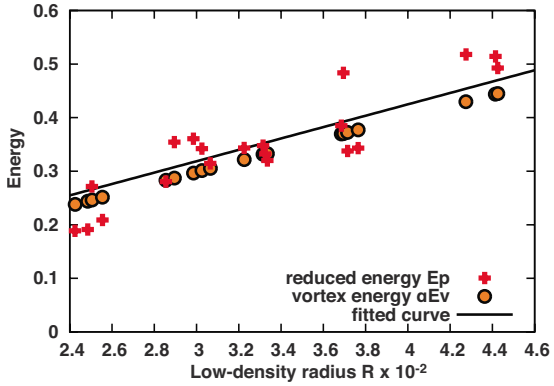

FIG. 11. (Color online) Comparison of reduced energy E_p with vortex energy E_v at $M_\infty=5$.

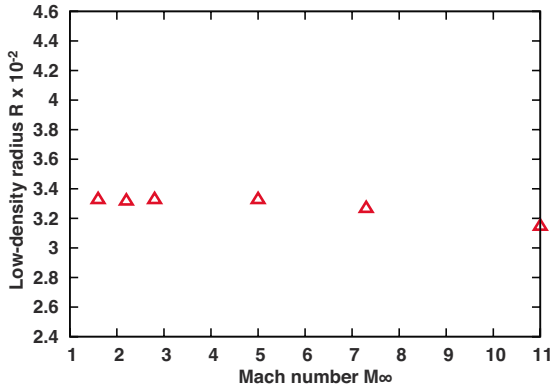

FIG. 12. (Color online) Relationship between low-density radius R and Mach number M_∞ with parameters $Q=4.29\times10^{-3}$ and $L=0.5$.

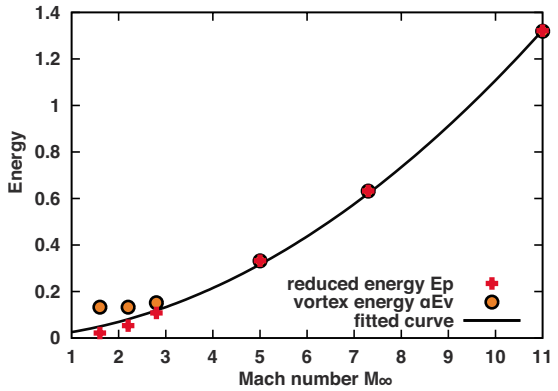

FIG. 14. (Color online) Comparison of reduced energy E_p with vortex energy E_v, with parameters $Q=4.29\times10^{-3}$ and $L=0.5$.

$$E_p \cong 14.5E_v = 10.0R, \tag{20}$$

while the fitted curve estimated from scattered reduced energies is slightly different from the above expression.

On the other hand, with the condition of $Q=4.29\times10^{-3}$ and $L=0.5$, we also clarified the dependence of reduced energies on the freestream Mach number. By substituting the Rankine–Hugoniot relation for the pressure-jump condition,

$$\gamma P_{\text{bow}} = \frac{\bar{P}_{\text{bow}}}{P_\infty} = 1 + \frac{2\gamma}{\gamma+1}(M_\infty^2 - 1), \tag{21}$$

for Eq. (18), we used

$$\omega_z = \frac{2\delta}{\gamma+1}(1-\rho_{\text{low}})\left(M_\infty - \frac{1}{M_\infty}\right)\frac{1}{R^2}. \tag{22}$$

The vortex energy E_v was then expressed by

$$E_v = \frac{8}{3}\left(\frac{\pi}{\gamma+1}\right)^2(1-\rho_{\text{low}})^2 R\left(M_\infty - \frac{1}{M_\infty}\right)^2\delta^2. \tag{23}$$

Figure 12 plots the relationship between low-density radius and Mach number in a constant deposition condition. Note that the time intervals between the energy deposition and the beginning of interaction differ depending on the freestream velocity. Since the low-density radius R weakly depended on Mach number M_∞, we can assume the radius R was constant over variations of Mach number. Figure 13 compares the computed shock stand-off distance δ with Billig's values of δ.[21,22] A simple correlation for the shock stand-off distance of sphere-cone bodies proposed by Billig is given by $\delta=7.15\times10^{-2}\exp(3.24/M_\infty^2)$. Therefore, we employed this formula for Eq. (23). Figure 14 indicates the results of reduced energy E_p and vortex energy αE_v with various Mach numbers. We found very good agreement between them with $\alpha=14.5$. From this result, the other forms of E_p explicitly written as a function of Mach number could be expressed using Billig's formula:

$$E_p \cong 14.5E_v = 2.2\left(M_\infty - \frac{1}{M_\infty}\right)^2\delta^2 = 1.13\times10^{-2}\left(M_\infty - \frac{1}{M_\infty}\right)^2\exp\left(\frac{6.48}{M_\infty^2}\right). \tag{24}$$

In particular, when the Mach number exceeds 3, they almost all correspond because of the "Mach independence" (Fig. 13). If the shock stand-off distance is not changed over the Mach number (which is true for high Mach number) (Fig. 13), the reduced energy E_p is proportional to the square of the Mach number from Eq. (24).

Considering the analysis by means of the baroclinic source term of vorticity mentioned above, we found a strong relationship between reduced energy E_p and vortex energy E_v. The vortex energy was proportional to the low-density radius R and the square of the freestream Mach number M_∞ [Eq. (23)]. These dependencies were clearly observed in the computational results of the reduced energy. These results suggested that the reduced energy must be predictable from the vortex energy estimated by the baroclinic term of Eq. (16), while the unknown constant α should be determined empirically.

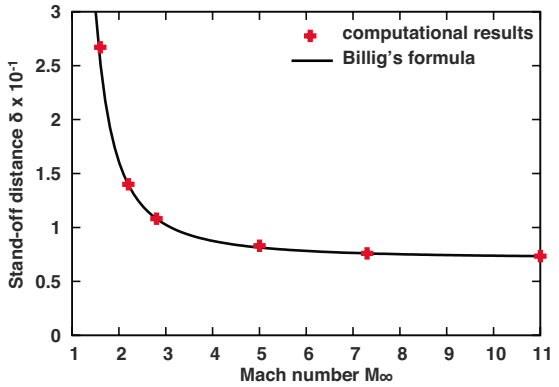

FIG. 13. (Color online) Comparison of stand-off distance δ between the computation and Billig's formula.

E. Wave drag reduction with low-entropy shock

Finally, we attempted to arrive at another interpretation of the physical mechanism of the drag reduction due to the unsteady hydrodynamic interaction phenomena between a bow shock wave over a blunt body and a low-density core produced by pulse energy deposition from the aspect of entropy reduction.

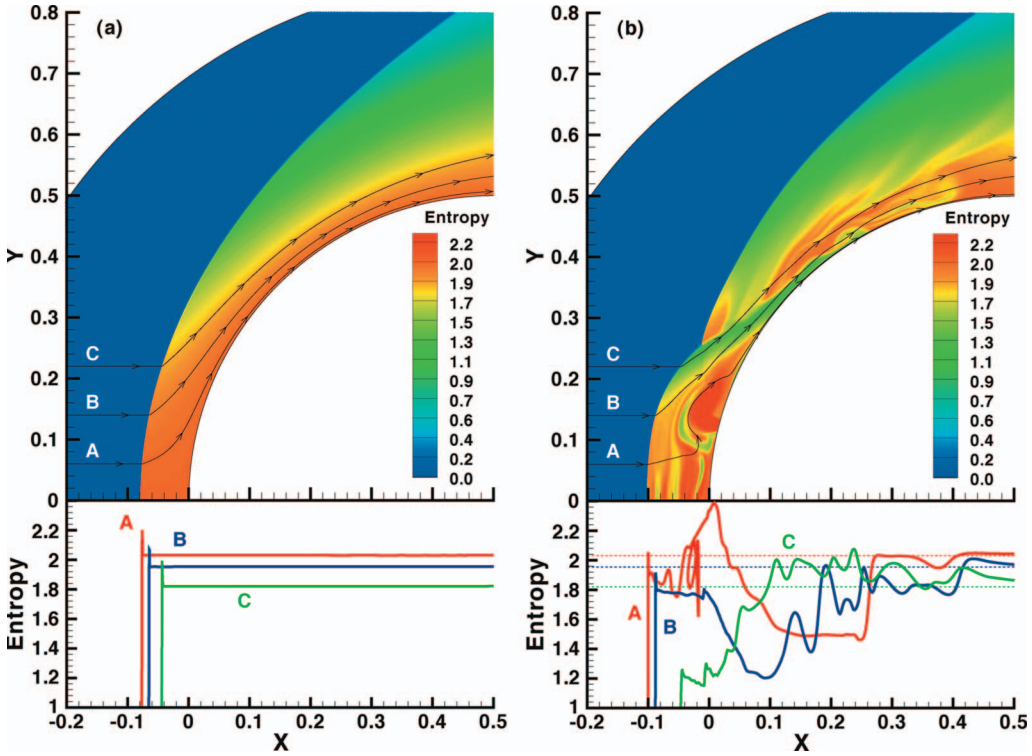

FIG. 15. (Color) Snapshots of the entropy distribution at $M_\infty=5$ measured from the freestream state (upper panel) and the extracted entropy profile along three stream traces A, B, and C (lower panel), (a) without pulse energy deposition and (b) with parameters $Q=4.29\times10^{-3}$ and $L=0.5$ at $t=0.325$.

Wave drag is attributed to entropy generation at the shock front. According to energy conservation, the ratio of the total pressure in front of shock wave $P_{t,\infty}$ to that behind it ($P_{t,\mathrm{bow}}$) becomes $P_{t,\mathrm{bow}}/P_{t,\infty}<1$ on the same stream line.[23] Here, the total pressure loss directly led to wave drag, and the entropy production was a counterpart of it:

$$\frac{S_{\mathrm{bow}}-S_\infty}{R_{\mathrm{air}}}=\ln\left(\frac{P_{t,\infty}}{P_{t,\mathrm{bow}}}\right), \tag{25}$$

where S denotes the entropy, and R_{air} is the gas constant of air.

Figures 15(a) and 15(b) present snapshots of the entropy distribution measured from the freestream state with $M_\infty=5$ (upper panel) and the extracted entropy profile along stream trace lines A, B, and C (lower panel), (a) without pulse energy deposition and (b) with the reference condition at $t=0.325$, corresponding to Figs. 2–4; (f). Comparison of these figures reveals that entropy increases because of vorticity existence, as described by the Crocco theorem in the low-density vortex region. However, the entropy was reduced more than that without interaction around the low-density vortex region (stream traces A and B) and the downstream region beginning from a kink in the distorted bow shock (stream trace C).

In the flow around the low-density core, the vortex produced by the interaction phenomena converted a part of the internal energy into kinetic energy of a fluid element. It was assumed that the converted energy corresponded to vortex energy αE_v generated by the baroclinic effect. Therefore, the total pressure $P_{t,\mathrm{bow}}$ locally became high, and the total pressure loss was suppressed. For the duration of the vortex advection in the bow shock layer, the entropy was kept at a lower value than that without energy deposition. In other words, the low-entropy shock, which was realized instantaneously, was the physical essence of the drag reduction mechanism based on purely hydrodynamic phenomena.

IV. CONCLUSION

The interaction flow field between a bow shock developed in front of a blunt body and a blast wave was numerically simulated in order to study the drag reduction effect of the blunt body by pulse energy deposition. The obtained results clarified that the vortex region generated by the unsteady hydrodynamic phenomena contributed significantly to drag reduction, and that the obtained reduced energy E_p considerably exceeded the deposited energy Q obtained in many previous studies.

The effects of deposited energy Q, deposition location L, and freestream Mach number M_∞ on energy reduction were examined in this parametric study. According to the computational results, the reduced energy E_p was proportional to the deposited energy. The deposition location contributed less to reduced energy because the low-density core induced by the energy deposition was still comparable in size to that just before the interaction in the parameter space considered in the present study. Additionally, the reduced energy E_p was proportional to the square of the relatively high freestream Mach number.

The drag was reduced more when the vortex region moving along the wall surface was larger or the freestream Mach number was higher. We focused on the baroclinic

source term of vorticity and refined the parameters for the reduced energy E_p. Computational results indicate the reduced energy linearly depends on vortex energy E_v, which can be theoretically predicted from the baroclinic effect. We then observed the linear dependence on the low-density radius R of the blast wave before interaction and proportional to the square of the freestream Mach number M_∞, as well as the computational results. Therefore, we could roughly estimate the value of the reduced energy from the size of the blast wave before interaction and the freestream Mach number. We have suggested that the obtained theoretical expression and knowledge from the baroclinic effect provide beneficial information on drag reduction by a pulse energy deposition. The proportionality factor $\alpha=14.5$ was found through the use of numerical simulations with the characteristic parameters, while it was not as easy to estimate its specific value from only the simple evaluation that we conducted. Thus, estimating the factor α concretely will require more careful treatment of the pressure gradient ∇P in the baroclinic term and the volume of the low-density vortex core. The applicable parameter space of the relation between E_p and E_v is the situation wherein the diameter of sphere d exceeds the low-density radius ($R=\bar{R}/d<10^{-1}$).

We have presented a qualitative discussion of the relationship between vortex formation and entropy production described by the Crocco theorem. From the perspective of entropy suppression at the shock front due to vorticity generation, it was assumed that pulse energy deposition was a technique of low-entropy shock formation using the unsteady fluid motion driven by hydrodynamic instability. If we used the blast wave as a seed of the perturbation with the deposition of low energy, large reduced energy was assured in this sense. Actually, some experimental results suggested that the enhancement of the instability in the stagnation region led to efficient drag reduction.[11]

ACKNOWLEDGMENTS

We would like to thank Dr. Akihiro Sasoh and Dr. Koichi Mori for their effective introduction to this subject and for their suggestions from their experiments. We greatly appreciate the valuable discussions with Dr. Michiko Furudate and Mr. Masami Tate, as well as their technical help with computations. This work was partly supported by a Grant-in-Aid from the Japan Society for the Promotion of Science Fellows and the Program for Improvement of Research Environment for Young Researchers from Special Coordination Funds for Promoting Science and Technology (SCF) commissioned by the Ministry of Education, Culture, Science, and Technology (MEXT) of Japan.

[1] S. M. Bogdonoff and I. E. Vas, "Preliminary investigations of spiked bodies at hypersonic speeds," J. Aerosp. Sci. **26**, 65 (1959).
[2] D. H. Crawford, "Investigations of the flow over a spiked-nose hemisphere-cylinder at a Mach number of 6.8," NASA Report No. TN D-118, Langley Research Center, 1959.
[3] D. J. Maull, "Hypersonic flow over axially symmetric spiked bodies," J. Fluid Mech. **8**, 584 (1960).
[4] D. M. Bushnell, "Supersonic aircraft drag reduction," AIAA Paper No. 90-1596, 1990.
[5] L. N. Myrabo and Y. P. Raizer, "Laser-induced air spike for advanced transatmospheric vehicle," AIAA Paper No. 94-2451, 1994.
[6] D. W. Riggins, H. F. Nelson, and E. Johnson, "Blunt-body wave drag reduction using focused energy deposition," AIAA J. **37**, 460 (1999).
[7] R. Takaki and M.-S. Liou, "Parametric study of heat release preceding a blunt body in hypersonic flow," AIAA J. **40**, 501 (2002).
[8] R. Kandala and G. V. Candler, "Numerical studies of laser-induced energy deposition for supersonic flow control," AIAA J. **42**, 2266 (2004).
[9] R. G. Adelgren, H. Yan, G. S. Elliott, D. D. Knight, T. J. Beutner, and A. A. Zheltovodov, "Control of Edney IV interaction by pulsed laser energy deposition," AIAA J. **43**, 256 (2005).
[10] K. Mori and A. Sasoh, "Experiments of laser-pulse-induced drag modulation in supersonic flow," AIAA Paper No. 2006-3569, 2006.
[11] T. Sakai, Y. Sekiya, K. Mori, and A. Sasoh, "Interaction between laser-induced plasma and shock wave over a blunt body in a supersonic flow," J. Aerosp. Eng. **222**, 605 (2008).
[12] P. Y. Georgievskii and V. A. Levin, "Unsteady interaction of a sphere with atmospheric temperature inhomogeneity at supersonic speed," Fluid Dyn. **28**, 568 (1993).
[13] P. Y. Georgievsky and V. A. Levin, "Bow shock waves structures control by pulse-periodic energy input," AIAA Paper No. 2004-1019, 2004.
[14] A. A. Zheltovodov, E. A. Pimonov, and D. D. Knight, "Energy deposition influence on supersonic flow over axisymmetric bodies," AIAA Paper No. 2007-1230, 2007.
[15] R. D. Richtmyer, "Taylor instability in shock acceleration of compressible fluids," Commun. Pure Appl. Math. **13**, 297 (1960).
[16] E. E. Meshkov, "Instability of the interface of two gases accelerated by a shock wave," Fluid Dyn. **4**, 101 (1969) (translated from Izv. Akad. Nauk SSSR, Mekh. Zhidk. Gaza **4**, 151 (1969).
[17] A. Sasoh, T. Ohtani, and K. Mori, "Pressure effect in a shock-wave-plasma interaction induced by a focused laser pulse," Phys. Rev. Lett. **97**, 205004 (2006).
[18] Y. Wada and M. S. Liu, "A flux splitting scheme with high-resolution and robustness for discontinuities," AIAA Paper No. 94-0083, 1994.
[19] B. Van Leer, "Towards the ultimate conservative difference scheme. V. A second-order sequel to Godunov's method," J. Comput. Phys. **32**, 101 (1979).
[20] L. I. Sedov, *Similarity and Dimensional Methods in Mechanics* (CRC, Boca Raton, 1993).
[21] F. S. Billig, "Shock-wave shapes around spherical- and cylindrical-nosed bodies," J. Spacecr. Rockets **4**, 822 (1967).
[22] J. D. Anderson, Jr., *Hypersonic and High Temperature Gas Dynamics* (McGraw-Hill, New York, 1989).
[23] H. W. Liepmann and A. Roshko, *Elements of Gasdynamics* (Wiley, New York, 1957).